Journal of Applied Fluid Mechanics, Vol. 17, No. 6, pp. 1322-1338, 2024.
Available online at www.jafmonline.net, ISSN 1735-3572, EISSN 1735-3645.
https://doi.org/10.47176/jafm.17.6.2251

Numerical Analysis of Film Cooling Flow Dynamics and Thermodynamics for Perfect and Imperfect Cooling Holes

S. Liang, R. L. Dong†, W. W. Xu and Y. Q. Wei

Department of Fluid Engineering, Zhejiang Sci-Tech University, Hangzhou 310018, China

†*Corresponding Author Email: dongruoling@zstu.edu.cn*

ABSTRACT

Film cooling protects high-temperature components and generates complex vortex structures through the interaction between the mainstream flow and the injected coolant. Additionally, the process of applying thermal barrier coatings introduces imperfect cooling holes. A numerical simulation study is conducted on two geometric configurations: inclined perfect and imperfect holes arranged in a single row on a flat plate to investigate the effects of flow field vortex structures and hole imperfections. The k-epsilon turbulent model is employed to analyse the impact of varying blowing ratios and defect positions on flow field structure and cooling efficiency, with vortex dynamics providing explanatory insights. As the blowing ratio increases, the kidney vortex associated with the perfect holes progressively detaches from the wall, reducing film cooling efficiency. The kidney vortex originates from the shear interaction between the mainstream and the impinging jet, predominantly influenced by the vortex stretching component. Imperfect holes influence the distribution state of the kidney vortex, with weakened roll-up phenomena observed at the IT4 defect location. Consequently, a noticeable enhancement in film cooling effectiveness is achieved near the proximal end of the hole.

Article History

Received August 18, 2023
Revised December 23, 2023
Accepted January 9, 2024
Available online March 27, 2024

Keywords:

Film cooling
Kidney vortex
Vortex dynamic
Adiabatic cooling effectiveness

1. INTRODUCTION

With the gradual advancement of aero-engine technology, there has been a discernible trend towards elevated turbine inlet temperatures. This phenomenon is attributed to the improved efficiency of the gas turbines with increasing temperature. It is imperative to adopt efficient cooling mechanisms to avert the risk of overheating and subsequent melting of the turbine's hot-end components. Film cooling has emerged as a pivotal technique for cooling turbine blades. The film cooling process involves injecting cooling jets through small holes into the blade surface, creating a protective low-temperature layer that shields the blade from excessive thermal loading. Thermal barrier coatings (TBCs) enhance film-cooling efficacy and further augment the hot-end components' heat-bearing capacity. This strategy represents a viable pathway for overcoming the technological bottlenecks that limit the reliability of hot-end components in next-generation high-performance aerospace engines (Bunker, 2005).

Extensive research has been conducted on various factors that influence film cooling. To elucidate the mechanisms and flow-field structures underlying film cooling, it was revealed that the flow-field structure significantly influences film cooling efficiency. Numerical simulations were performed for circular holes that were oriented streamwise. The simulations revealed the presence of kidney vortices downstream of the jet exit. Additionally, it was observed that reducing the strength of symmetric vortex pairs led to a notable improvement in the film-cooling efficiency (Walters & Leylek, 1997; Andreopoulos & Rodi, 1984; Sykes et al., 1986).

Various methods are commonly employed to mitigate the impact of kidney vortices, including modifications to the inlet shape, angle, length, and external factors, such as the blowing ratio and turbulence intensity. These adjustments are aimed at altering the kidney vortex structure to affect the cooling efficiency (Funazaki, et al., 2013; Wu et al., 2016; Chang, et al., 2019; Zhang, et al., 2020).

Lim et al. (2001) explored the flow structure in the near field of free jets by introducing fluorescein dye into a circulating water channel. The presence and origin of the counter-rotating kidney vortex pairs were investigated. These kidney vortices significantly impact downstream cooling efficiency, leading to the adoption of various methods to mitigate their effects. Heidmann and Ekkad (2008) designed a counter-vortex hole that effectively

NOMENCLATURE

D	hole diameter	ρ	fluid density
M	blowing ratio	h	enthalpy
Re	Reynolds number	μ	molecular and turbulent viscositiy
U	mean velocity	p	pressure
T_∞	mainstream temperature	x	streamwise coordinates
T_c	incident flow temperature	y	vertical coordinates
T_{aw}	adiabatic wall temperature	z	spanwise coordinates
VS	streamwise vorticity stretching component	μ_t	turbulent viscosity
P_r	molecular Prandtl number1	y^+	normalized distance from the wall
σ_h	turbulent Prandtl number	η	film cooling effectiveness
Γ_u	momentum coefficient	$\overline{\eta}$	average adiabatic film cooling effectiveness
Γ_h	thermal diffusion coefficient	η_{av}	Film cooling spanwise effectiveness
$\boldsymbol{\omega}$	vorticity	u_∞	mainstream average inlet velocity

counteracted the detrimental vortices associated with standard round holes and maintained them on the surface. Zhang and Zhu (2020) proposed a novel arrangement of auxiliary holes interleaved with the main holes on a flat plate to enhance the film cooling effectiveness. The numerical results indicated that the large-scale vortices induced by the auxiliary holes suppressed the downstream development of the main hole's kidney anti-symmetric vortices. Jiang et al. (2020) designed various coolant-delivery structures to mitigate the impact of kidney vortices and conducted comparative studies at different blowing ratios. The results revealed the formation of strong kidney vortices outside the film cooling holes, particularly at high blowing ratios. Although they examined the influence of delivery structures on kidney vortices, they did not analyse the underlying mechanisms. Panda et al. (2023) compared two standard convective cooling methods–jet impingement and film cooling–and evaluated different heat transfer parameters for both cases. Film cooling exhibited superior heat flux and Nusselt numbers on the interacting surface compared to jet impingement cooling. Chen et al. (2019) conducted numerical simulations to investigate the influence of crossflow within internal cooling channels on film-cooling performance. They proposed a theoretical model for the boundary layer deformation based on vortex dynamics to explain the formation of internal hole vortices.

Owing to its effective cooling capabilities, film cooling has been widely applied. However, practical applications still pose numerous challenges, including imperfections during hole fabrication and thermal barrier coating applications. A comparison between the cases with and without imperfect holes revealed that defects alter the formation of vortex structures, and defects at the hole exit enhance the film-cooling effectiveness. These observations were confirmed through experiments conducted using a water tank setup, where the working fluid was room-temperature liquid water at temperatures of 20°C and 26°C. (Jovanovic´ et al., 2005, 2006, 2008). In typical gas turbine airflows, the temperature ratio falls within the range of 0.5 to 0.85, while the blowing ratio varies from 0.3 to 2.0 (Han et al., 2013). Bunker (2014) conducted experimental research on the influence of semicircular hole imperfections on jet cross-flow interactions using particle image velocimetry and liquid-crystal thermography techniques. Nemdili et al. (2011) conducted numerical simulations of the interaction between a jet and a crossflow in the presence of defects inside the jet holes using liquid water at room temperature. Their research focused on the effect of defect size, revealing that as the defect size increased, the distance of the centre of the kidney vortex from the wall also increased. Rezzag and Jubran, (2019) used room-temperature liquid water for their numerical simulations. They observed that under different blowing ratios, the tilt angle of the hole significantly affected the film-cooling efficiency. However, they did not investigate the effect of hole placement or the mechanism of vortex formation. Huang et al. (2018) conducted experimental research using specialised pyramid-shaped elements to simulate the internal imperfections of holes. The study demonstrated that hole blockage significantly influences film-cooling effectiveness and the discharge coefficient. Although they focused on pyramid-shaped defects, they did not analyse the influence of vortex structures on film cooling. Tian et al. (2018) investigated and analysed two similar blockage ratios with different defect shapes: hemispheres and tetrahedrons. Their results revealed that the lateral film cooling efficiency of the hemispherical blockage structure was lower than that of the tetrahedral structure.

Based on the literature review, kidney vortices' presence significantly influences the downstream flow field structures and cooling effects, similar to the effects observed with imperfect holes. However, there has been limited exploration of the generation and evolution of these vortices.

This study employed numerical simulations to analyse the flow characteristics under different blowing ratios for circular hole configurations on a flat plate. In addition, a vortex transport equation was used to explain vortex generation. Furthermore, this study investigated the variations between semicircular imperfect holes at four different positions and perfect holes in the upper kidney vortex structure. Ultimately, this study aimed to determine the most reasonable defect location and optimal cooling efficiency. Concurrently, this numerical study involved

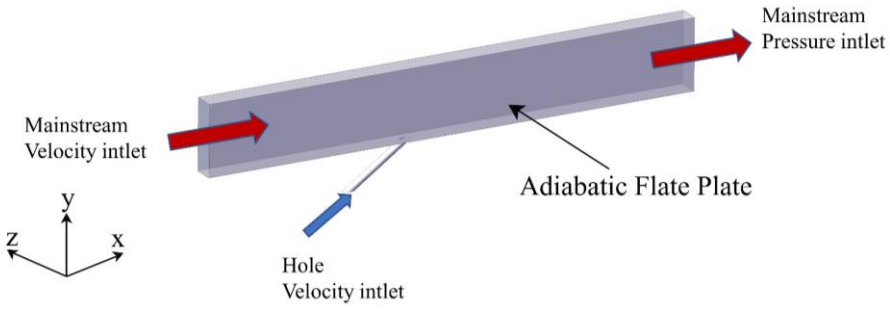

Fig. 1 Computational Domain

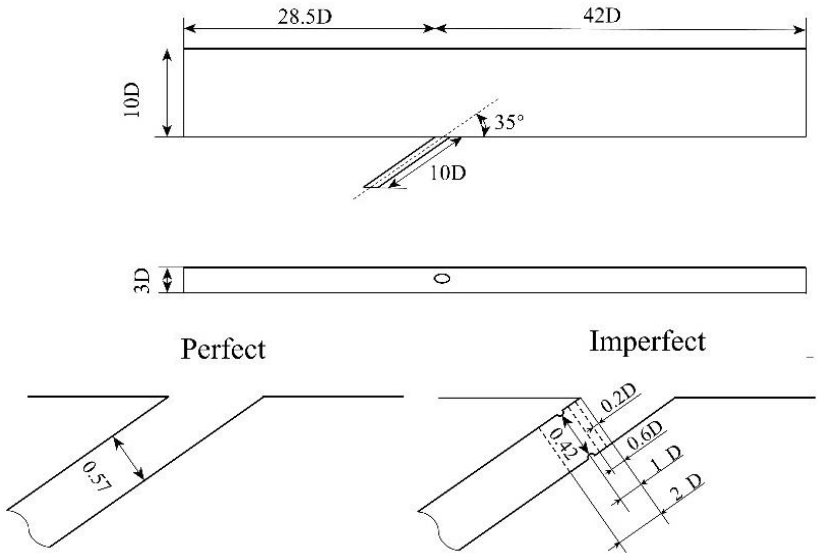

Fig. 2 Geometric Dimensions of the Computational Model

simplifying a gas turbine model to investigate the interaction between the transverse and jet flows of perfect and imperfect holes and the formation of vortices. These flow characteristics correspond to film cooling in gas turbines.

2. COMPUTATIONAL MODEL AND METHODOLOGY

2.1 Geometrical Configuration

The 3D computational model used in this numerical simulation study is based on Jovanic's experimental setup (Jovanović et al., 2008). The computational domain is depicted in Fig. 1 and is divided into two main components: the mainstream channel and the film cooling holes. The dimensions of the numerical model are shown in Fig. 2. Specifically, the diameter of the film cooling hole is D = 0.57 mm, the distance from the mainstream inlet to the front end of the film cooling hole is 28.5D, the distance from the mainstream outlet to the front end of the film cooling hole is 42D, the height of the mainstream channel is 10D, the inclination angle of the film cooling hole for the mainstream flow direction is 35°, the width of the film cooling hole is 3D. The length-to-diameter ratio (L/D) of the film cooling hole is 10. The origin was located at the front end of the film cooling hole, and the x, y, and z coordinate axes corresponded to the streamwise, wall-normal, and spanwise directions, respectively.

The dimensions of the selected computational domain were scaled to maintain the same Reynolds number as the experimental conditions based on the hole diameter and the distance from the plate's leading edge to the hole front. The boundary conditions for the computational domain were configured as follows: the mainstream inlet was set as the velocity inlet, and the mainstream outlet was specified as the pressure outlet. The mainstream average velocity u_∞ was 20 m/s and followed a velocity distribution with a 1/7 power-law exponent. The mainstream temperature T_∞ was 293.15 K, and the turbulence intensity was set at 1%. This study determined the secondary flow's inlet velocity by calculating the blowing ratio, ranging from 0.3 to 1.2. The inlet temperature of the secondary flow was 299.15 K. The flow pressure was set to standard atmospheric pressure to prevent a phase change in the liquid water. The lateral boundaries of the main channel were set as periodic boundary conditions, and all other boundaries were considered non-slip adiabatic walls. Both the mainstream and secondary flows were considered incompressible water. A second-order upwind scheme was used to

discretise the Navier-Stokes equations. Convergence is determined when the residuals of all equations are smaller than 10^{-5} , and the residual curves show no further decrease.

2.2 Numerical Method and Governing Equations

Because of the fluid's incompressible nature in this study's numerical simulation, the working fluid was assumed to be a Newtonian fluid with temperature-dependent properties. Thus, the conservation equations for the mass ($\partial U_i / \partial x_i = 0$),momentum, and energy are presented in a concise Cartesian tensor notation (Lakehal et al., 2001), and they are solved numerically using the finite volume method:

$$\frac{\partial}{\partial x_j}\left[\rho U_i U_j - \Gamma_u\left(\frac{\partial U_i}{\partial x_j}+\frac{\partial U_j}{\partial x_i}\right)\right] = -\frac{\partial p}{\partial x_i} \tag{1}$$

$$\frac{\partial}{\partial x_j}\left[\rho U_j h - \Gamma_h\left(\frac{\partial h}{\partial x_j}\right)\right] = 0 \tag{2}$$

Where U_i , h , p , and ρ represent velocity, enthalpy, pressure, and fluid density components, respectively, and $\Gamma_u = (\mu + \mu_t)$ and $\Gamma_h = (\mu / P_r) + \mu_t / \sigma_h$ are momentum and thermal diffusion coefficients. μ and μ_t denote molecular and turbulent viscosities, and P_r and σ_h represent molecular and turbulent Prandtl numbers.

In this study, the flow is turbulent under the conditions above due to the high Reynolds number. Based on the reference from the literature above, the k - ε model with enhanced wall treatment is the optimal choice for predicting film cooling flow, and the predicted cooling effectiveness observed was in excellent agreement with experimental results. Therefore, the enhanced wall treatment k - ε model is adopted in the experimental model of this paper. The turbulent viscosity μ_t is calculated using the Realizable k - ε turbulence model, and it is related to the turbulent kinetic energy k and dissipation rate ε as follows:

$$\mu_t = \rho C_\mu \frac{k^2}{\varepsilon} \tag{3}$$

The transport equations are as follows:

$$\frac{\partial}{\partial x_i}\left(\rho U_i k - \Gamma_k \frac{\partial k}{\partial x_j}\right) = u_i\left(\frac{\partial U_i}{\partial x_j}+\frac{\partial U_j}{\partial x_i}\right)\frac{\partial U_i}{\partial x_j} - \rho\varepsilon \tag{4}$$

$$\frac{\partial}{\partial x_i}\left(\rho U_j \varepsilon - \Gamma_\varepsilon \frac{\partial \varepsilon}{\partial x_j}\right) = \rho C_1 S\varepsilon - \rho C_2 \frac{\varepsilon^2}{k+\sqrt{\nu\varepsilon}} \tag{5}$$

Where:

$$C_1 = \max[0.43, \frac{\zeta}{\zeta+5}], C_2 = 1.9, \zeta = S\frac{k}{\varepsilon} \tag{6}$$

$$S_{ij} = \frac{1}{2}\left(\frac{\partial U_i}{\partial x_j}+\frac{\partial U_j}{\partial x_i}\right), S = \sqrt{2S_{ij}S_{ij}} \tag{7}$$

2.3 Parameter Definitions

Several parameters are defined in this paper:

$$R_e = \frac{\rho_\infty U_\infty D}{\mu} \tag{8}$$

In the equation, R_e represents the Reynolds number, ρ_∞ is the density of the mainstream flow, U_∞ is the velocity of the mainstream flow, D is the diameter of the film cooling hole, and μ is the dynamic viscosity.

$$\eta = \frac{T_\infty - T_{aw}}{T_\infty - T_c} \tag{9}$$

$$\eta_{av} = \frac{1}{\Delta z}\int_{-\Delta z/2}^{\Delta z/2}\eta(x,z)\mathrm{d}z \tag{10}$$

In the equation, η represents the local adiabatic film cooling effectiveness, η_{av} is the spanwise-averaged adiabatic film cooling effectiveness, T_∞ is the mainstream temperature, T_c is the incident flow temperature, and T_{aw} is the adiabatic wall temperature.

$$M = \frac{\rho_c V_c}{\rho_\infty V_\infty} \tag{11}$$

where M represents the blowing ratio, ρ_∞ represents the density of the mainstream flow, V_∞ represents the velocity of the mainstream flow, ρ_c represents the density of the incident flow, and V_c represents the velocity of the incident flow. The blowing ratio essentially represents the velocity ratio because of the identical densities of the mainstream and injection flows. Under the reference experimental conditions, in which the mainstream velocity remained constant, any alteration in the blowing ratio was driven solely by changes in the injection flow velocity.

2.4 Grid Independence and Validation

This study used the commercial software ICEM for block-structured mesh generation in the computational domain. As depicted in Fig. 3, grid partitions were established for perfect and imperfect film-cooling hole configurations. Tetrahedral meshes were utilised, and grid refinement was implemented near the film-cooling holes and wall surfaces to ensure accuracy. A maximum wall-normal spacing $y^+ < 1$ with a wall-normal expansion ratio of 1.1 was employed for grid growth in the near-wall region.

Grid independence verification was conducted to obtain highly accurate computational results while conserving computational resources, as shown in Fig. 4.

Four grid quantities were employed:88w, 128w, 175w, and 229w. It was observed that the computational

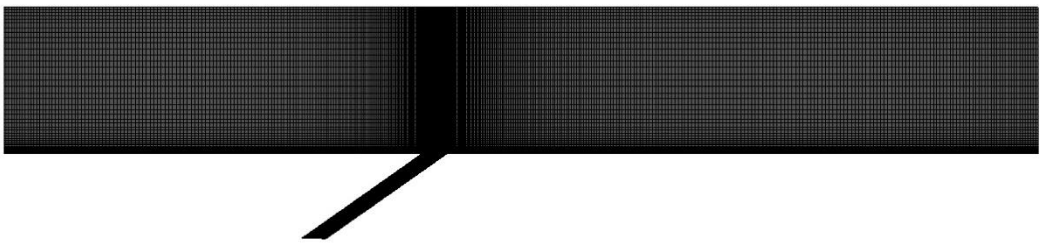

(a) Global Mesh

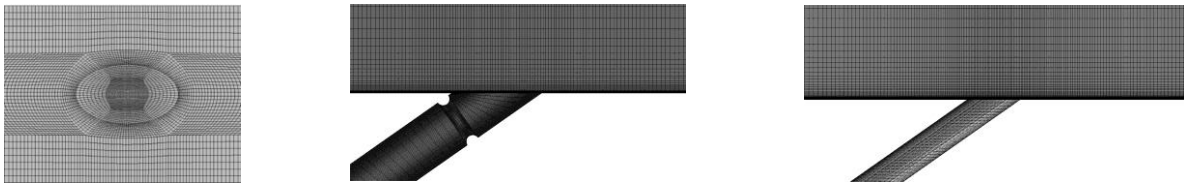

(b) Local Mesh

Fig. 3 Calculation Model Meshing for Perfect and Imperfect Holes

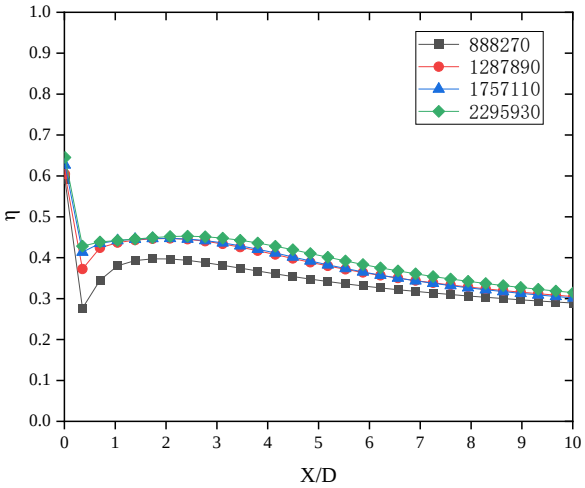

Fig. 4 Grid Independence Verification

model with 80w grid cells exhibited significant discrepancies compared with the others. As the grid size reached 175w, the downstream centreline adiabatic film-cooling effectiveness demonstrated minimal sensitivity to further increases in the grid cells. Consequently, this grid size was selected for the subsequent case analysis.

This study compared the wall centreline and spanwise-averaged film-cooling effectiveness to validate the accuracy of the numerical simulation results at a blowing ratio of M = 0.45 with the data from Jovanic and Roberg, as shown in Fig. 5. Additionally, we separately investigated three different turbulence models: Realizable k-ε (RKE), Standard k-ε (SKE), SST k-ω (SKW). This facilitates a more straightforward comparison of the cooling efficiency results between different turbulence models and experimental values. Given that the numerical simulation results of the Realizable model can well predict medium-scale vortices in film cooling and not only exhibit similar trends to experimental data but also closely match experimental results, we ultimately selected the Realizable k-ε turbulence model for subsequent studies.

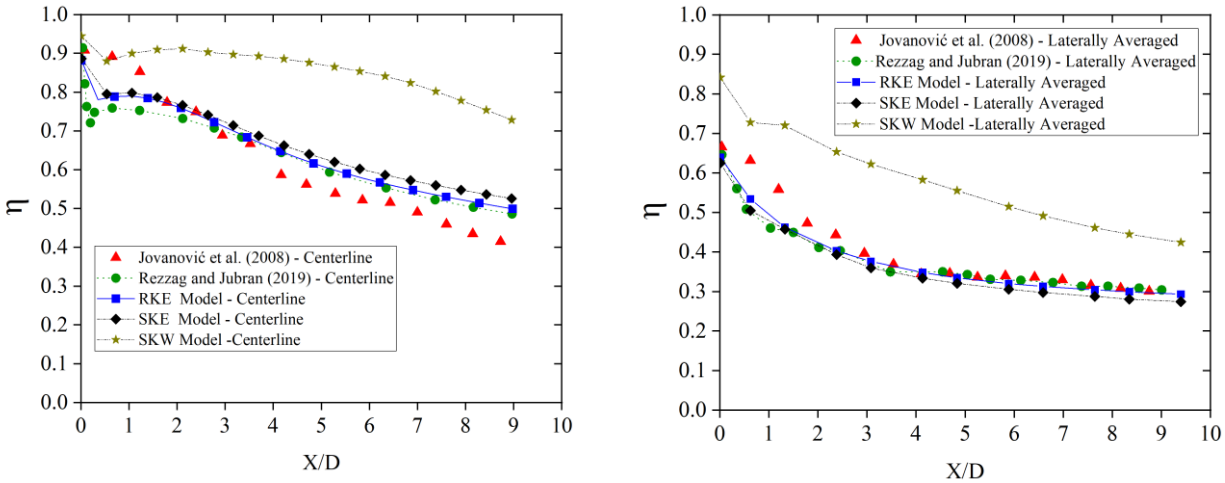

(a) Comparison of Wall Centerline Film Cooling Effectiveness

(b) Comparison of Spanwise-Averaged Wall Film Cooling Effectiveness

Fig. 5 Comparison of Film Cooling Effectiveness Simulation Results with Experimental Data

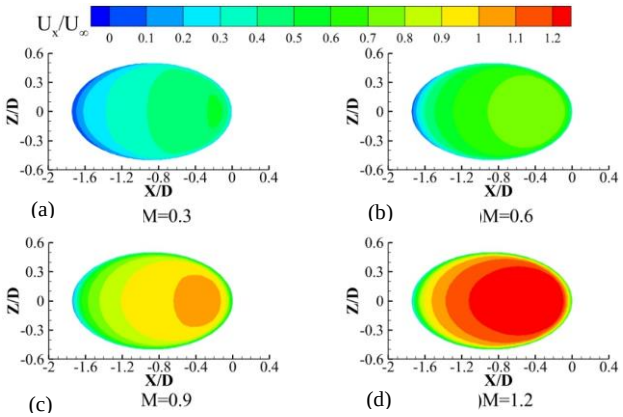

Fig. 6 X-direction Velocity Distribution at the Outlet Section of the Perfect Hole under Different Blowing Ratios

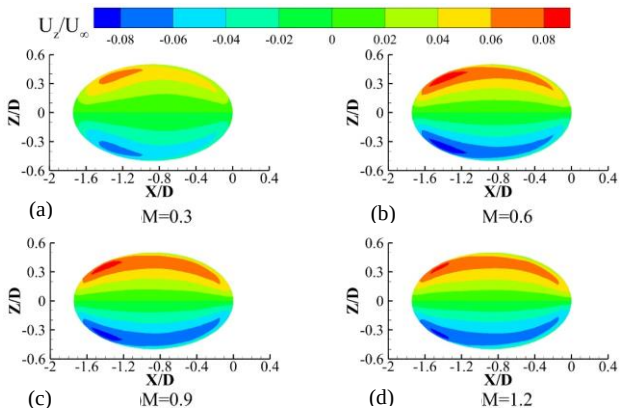

Fig. 8 Z-direction Velocity Distribution at the Outlet Section of the Perfect Hole under Different Blowing Ratios

3. RESULTS AND ANALYSIS

3.1 Flow Characteristics of Perfect Holes at Different Blowing Ratios

This section discusses the flow characteristics of a perfect hole configuration for different blowing ratios. Figures 6–8 show the velocity distributions in the X, Y, and Z directions, respectively, at the outlet section of the perfect hole. The velocity distribution at the outlet significantly affected the downstream film-cooling effectiveness and the vortex stretching term, as discussed below.

The X-direction velocity distribution in Fig. 6 shows that as the blowing ratio increased, the X-direction velocity also increased gradually for the perfect hole configuration. The outlet region exhibited increased velocity from left to right in the x-direction. This phenomenon results from the complex momentum and heat transfer interactions between the turbulent boundary layer and the incident flow within the film-cooling hole, where the main flow and jet intersect. After the incident flow exits the film-cooling hole and interacts with the mainstream, it deviates, reducing the turbulent boundary layer near the leading edge of the film hole (at X/D=-1.67).

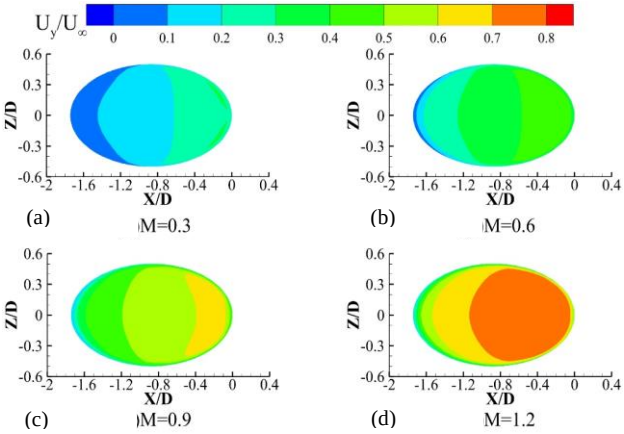

Fig. 7 Y-direction Velocity Distribution at the Outlet Section of the Perfect Hole under Different Blowing Ratios

Simultaneously, as the effect of the turbulent boundary layer of the mainstream weakened, the film-cooling efflux concentrated more at the rear of the film-cooling hole, reaching a maximum near the trailing edge of the hole and approaching the incident velocity.

The Y-direction velocity distribution in Fig. 7 exhibits a pattern of variation similar to that in Fig. 6 but with slightly decreased velocity magnitudes. The Z-direction velocity distribution in Fig. 8 exhibits a significant reduction in the velocity magnitude and noticeable changes in the distribution. The film-cooling hole region is symmetrically distributed in the spanwise direction (Z-direction) with opposing velocities, forming an asymmetric velocity distribution. This asymmetric distribution became less prominent when the blowing ratio was 0.6.

An increase in the X-direction velocity is beneficial for promoting streamwise film spreading. An increase in the Y-direction velocity aids the upward motion of the jet, enhancing its ability to penetrate the mainstream. An increase in the Z-direction velocity was advantageous for the spanwise spreading ability of the film. However, at high blowing ratios, the higher spanwise velocities resulted in the formation of stronger kidney-shaped vortices.

Based on the above analysis, the velocity distribution at the outlet of a perfect hole is primarily influenced by the X- and Y-direction velocities, with minimal influence from the Z-direction velocity. As the blowing ratio increased, the streamwise development and ability of the film to penetrate the mainstream also strengthened, as shown in Fig. 9.

As depicted in Fig. 9, the streamlines and temperature contour maps at the midplane of the perfect hole exhibit varying patterns under different blowing ratios. With an increase in the blowing ratio, the Y-direction velocity at the outlet increased, enhancing the penetration of the incident jet into the mainstream, leading to a more pronounced downstream lifting phenomenon, which adversely affected the film-cooling efficiency. The graph shows that at blowing ratios of M = 0.3 and M = 0.6, the film remains attached to the wall near the film hole and

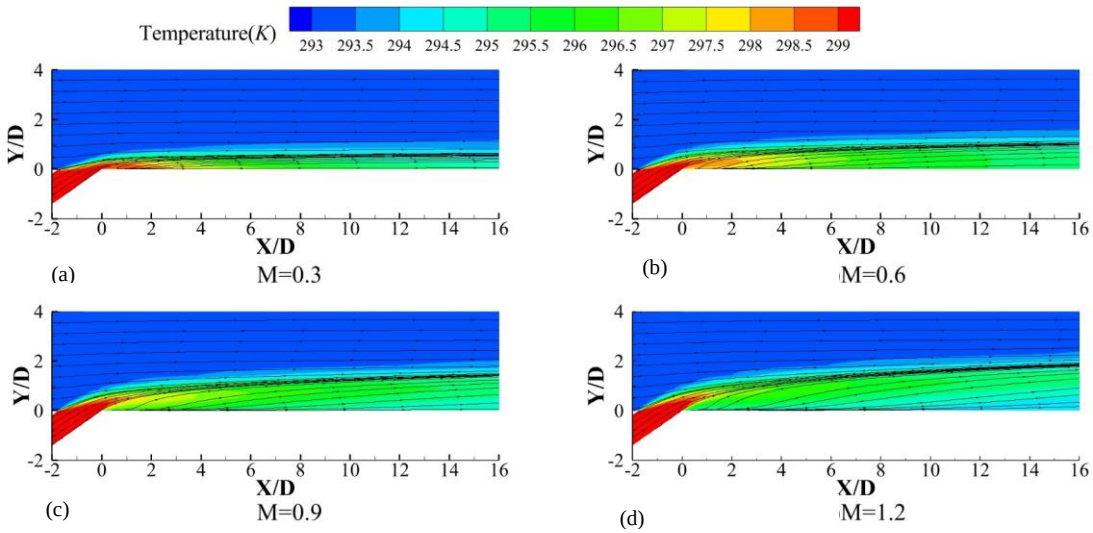

Fig. 9 Streamline and temperature contour plots at the central cross-section of the perfect hole under different blowing ratios

gradually detaches from the wall in the downstream region while maintaining effective film cooling. However, at blowing ratios of M = 0.9 and M = 1.2, the film can only remain attached to the wall near the film hole, and reattachment occurs downstream, resulting in a less favourable film coverage along the downstream wall. Moreover, as the blowing ratio increased, the reattachment phenomenon became more pronounced, decreasing film cooling efficiency.

A complex flow field formed as the incident jet flowed out of the film hole outlet and mixed with the mainstream. The interaction between the mainstream and incident jets resulted in a mutual influence. The incident jet obstructs the mainstream flow and, simultaneously, is itself affected by the mainstream, causing a diversion from its original direction. This phenomenon aligns well with the observations presented in Fig. 9. To examine the downstream flow development along the streamwise direction, Fig. 10 illustrates the temperature contour maps and velocity vector maps at the downstream cross sections with X/D values of 1, 3, and 5 for blowing ratios of M=0.3, 0.6, 0.9, and 1.2. It can be observed that owing to the pressure difference in the film hole outlet region, the outer layer of the incident jet is driven towards the centre of the wall, causing the surrounding mainstream to converge towards the wall, resulting in the incident jet forming a semicircular structure under various blowing ratios.

During downstream development, the action of kidney vortices affects the mixing of the mainstream and incident jets, directly influencing the cooling efficiency and coverage range. These vortices controlled the mixing downstream of the film hole. Kidney vortices are generated due to the mismatch in the vertical momentum between the mainstream and incident jets. They constitute a significant portion of the flow structure and play crucial roles. Moreover, they exert a wrapping effect on the mainstream, causing the mainstream to intrude into the lower part of the incident jet and enhancing the mixing between the incident jet and the mainstream.

Consequently, this weakened the protective effect of the incident jet on the wall. Therefore, kidney vortices have a significant impact on the downstream flow development. From Fig. 10, it can be observed that kidney vortices are formed under different blowing ratios for the perfect hole configuration. These vortices were initially close to the wall at the flow location X/D=1. As the flow progressed downstream, it gradually increased and detached from the wall at X/D=3 and 5. According to the above analysis, as the position of the kidney vortices increases, the mixing between the mainstream and incident jets becomes more intense, leading to a faster decrease in cooling efficiency. As the blowing ratio increased, the temperature contour distribution at the centre of the perfect hole changed from a completely elliptical shape to two separate elliptical distributions because of the increased X- and Z-direction velocities of the incident jet caused by the higher exitvelocity from the film hole at a high blowing ratio. The increased pressure difference pushed the incident jet toward the wall centreline, enhancing the entrainment effect of the kidney-shaped vortices. Consequently, the cooling efficiency at the centreline decreased for blowing ratios of 0.9 and 1.2. However, the increased Z-direction velocity improved cooling efficiency in the spanwise direction for lower blowing ratios (M=0.3, 0.6), leading to an increased region covered by the film.

3.2 Vortex Dynamics Analysis of the Perfect Hole Under Different Blowing Ratios

In the previous section, we analysed the distribution of outlet velocities in different directions for a perfect hole under different blowing ratios, downstream flow characteristics, and influence of kidney vortices. The velocity distribution and presence of kidney-shaped vortices significantly impact the downstream flow structure and film cooling efficiency.

Next, we investigated the variation in the vorticity downstream of the perfect hole under different blowing ratios. As established in a previous analysis, the exit flow of the injection jet was consistently affected by the

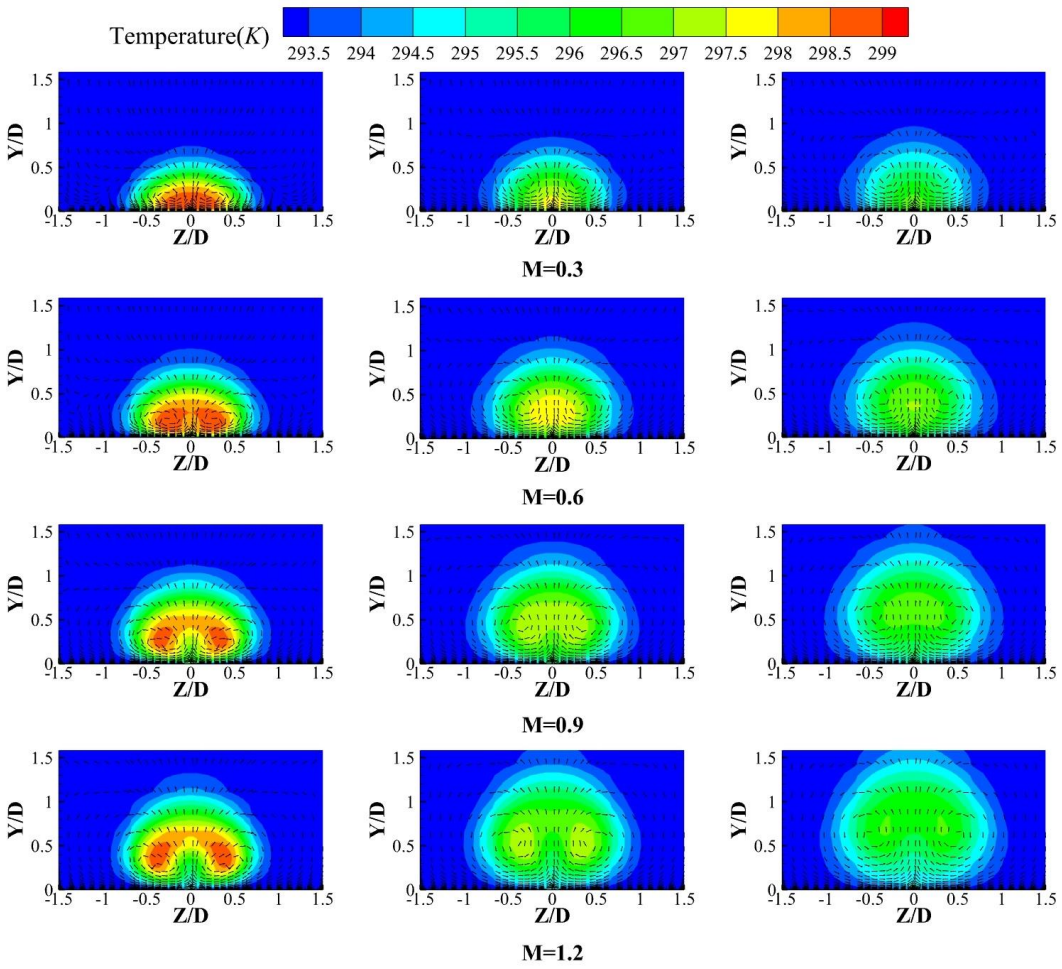

Fig. 10 Velocity vector and temperature contour plots at downstream cross-sections of the perfect hole under various blowing ratios (a: X/D=1, b: X/D=3, c: X/D=5)

presence of kidney-shaped vortices. The structure of these vortices significantly influences the downstream cooling efficiency of the hole exit; as they propagate downstream, they continue to contribute to the mixing of hot and cold flows, with their strength gradually diminishing along the streamwise direction. Figure 11 shows the development of these kidney vortices along the streamwise direction for different blowing ratios. The figures include vorticity maps at three selected streamwise positions to illustrate this development process, specifically at X/D = 0, 2, and 4.

As the blowing ratio increased gradually, the velocity at the outlet increased significantly, leading to an enhanced momentum of the exiting jet, resulting in the gradual intensification of the kidney vortices downstream of the film cooling hole. The position of the vortex core increased correspondingly. This phenomenon can also explain the change in the semicircular shape of the perfect hole in Fig. 10, as the increasing strength of the kidney vortex causes a shift in its cores' position, ultimately leading to a decrease in cooling efficiency. Furthermore, it can be observed that kidney vortices appear at the exit of the film-cooling hole for different blowing ratios. As the flow progresses downstream, the intensities of these vortices gradually decrease. In the case of high blowing ratios (M=0.9, 1.2), owing to the higher position of the vortex core, the decay process of the kidney vortex becomes slower, which undoubtedly hinders the improvement in the cooling efficiency. However, for lower blowing ratios (M=0.3, 0.6), the lowered position of the vortex core, influenced by the action of the vortices in the boundary layer near the wall, enhanced the decay of the kidney vortex. At M = 0.3, the intensity reached its lowest point.

Based on the analysis in the previous section, when the blowing ratio M = 0.6, the structure of the kidney vortex is visible, and the cooling effect is at its best. Therefore, the subsequent study focused only on M = 0.6, neglecting the influence of velocity variations on the downstream flow field vortex structure. A vortex identification method based on the Q-criterion was applied to the vortex flow field using the numerical simulations' results (Zhan et al., 2019). The Q-criterion method is based on the characteristic equation of the velocity gradient tensor.

$$\lambda^3 + P\lambda^2 + Q\lambda + R = 0 \tag{12}$$

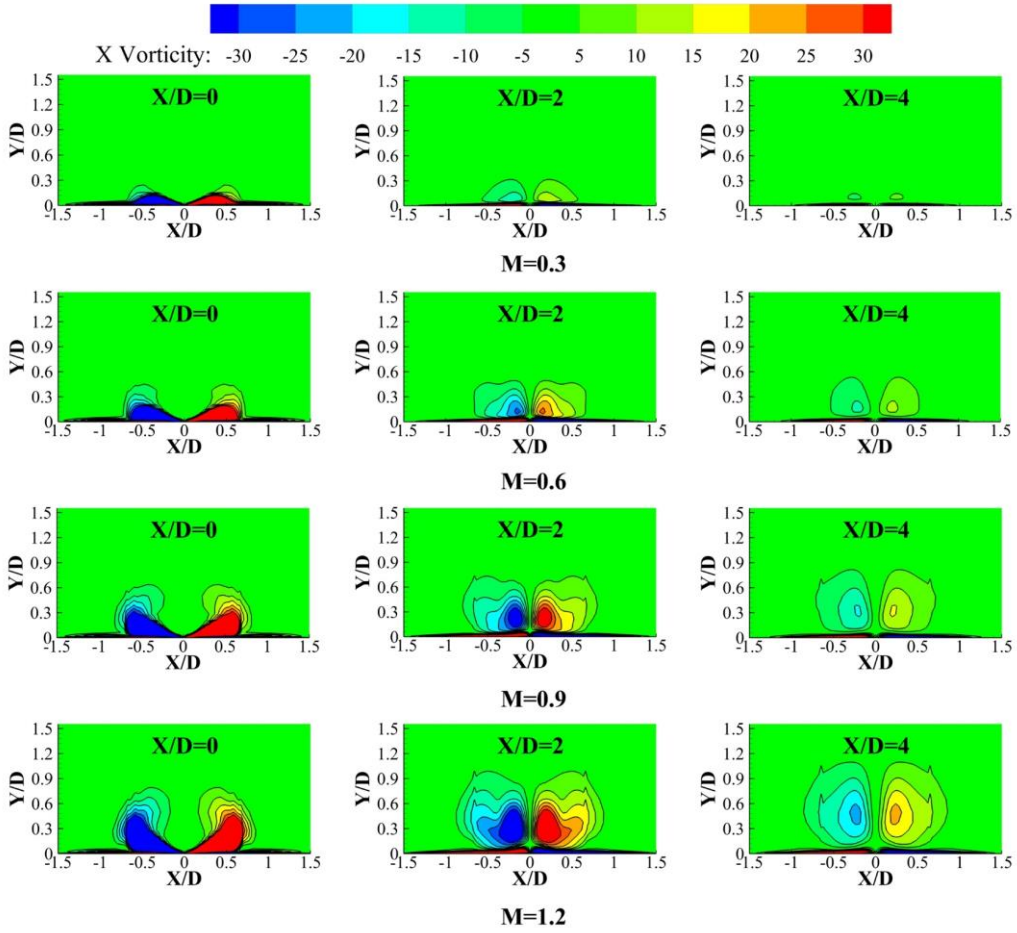

Fig. 11 Vorticity distribution at different streamwise locations X/D=0, 2, and 4 downstream of the perfect hole exit in the flow field of the perfect hole

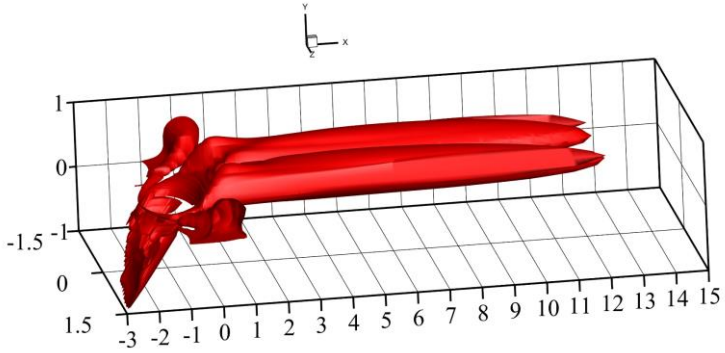

Fig. 12 Vorticity identification using the Q-criterion (Q=1) for the perfect hole at a blowing ratio of M=0.6

The region in which the second invariant of the velocity gradient tensor Q > 0 is identified as the vortex. In this context, the expression for Q is as follows:

$$Q = \frac{1}{2}(\| A \|_F^2 - \| S \|_F^2) \tag{13}$$

Where S represents the symmetric part of the velocity gradient tensor, and A represents the anti-symmetric part, corresponding to deformation and rotation in the flow field. The physical interpretation of the Q criterion is that the vorticity associated with rotational effects in the flow field is greater than that associated with deformation effects, indicating that the rotational effects dominate.

Figure 12 illustrates the visualisation of the vortical structures using the Q-criterion, with a value of 1 for a perfect hole at a blowing ratio of M = 0.6 During the film-cooling process of the injection jet exiting the hole, a horseshoe-shaped vortex formed near the wall near the hole exit. This vortex was wrapped around the outer region

of the injection jet along the mainstream flow direction. As the injection jet progressed downstream, it was influenced by the mainstream gas, forming a high-pressure region upstream of the gas. This pressure distribution causes the injection jet to bend owing to compression, and simultaneously, the shear force from the downward motion of the mainstream causes the initial single-vortex structure at the hole exit to evolve into a counter-rotating kidney vortex pair. Moreover, it can be observed that the vortex structure originates from the region near the hole exit, indicating that the vortex formation is primarily driven by the interaction between the injection jet and the mainstream, leading to the development of shear-layer vortices and the subsequent formation of kidney-shaped vortices.

Due to the intricate flow field resulting from the interaction of the mainstream and injection jets, where vortex structures govern the flow field, current research has predominantly focused on the post-analysis of vortices without investigating the underlying reasons for their formation. Thus, this section discusses film cooling vortex dynamics analysis based on the fluid particle vorticity transport equation. The vorticity transport equation is expressed as follows:

$$\frac{D\boldsymbol{\omega}}{Dt} = (\boldsymbol{\omega}\cdot\nabla)\boldsymbol{u} - \boldsymbol{\omega}(\nabla\cdot\boldsymbol{u}) + \frac{\nabla\rho\times\nabla p}{\rho^2} + \nabla\times\boldsymbol{F}_{visc} + \nabla\times\boldsymbol{X} \tag{14}$$

In the equation above, $\boldsymbol{\omega}$ represents vorticity,and $\boldsymbol{u}$ represents velocity, where the left-hand side of Eq.(12), denoted as $D\boldsymbol{\omega}/Dt$, signifies the rate of change of vorticity. On the right-hand side, $(\boldsymbol{\omega}\cdot\nabla)\boldsymbol{u}$ stands for vortex stretching (VS), indicating the stretching and bending of vortex lines due to velocity gradients in the flow field, consequently altering the magnitude and direction of vorticity. $\boldsymbol{\omega}(\nabla\cdot\boldsymbol{u})$ signifies vortex dilatation, arising from changes in the volume of fluid elements, leading to changes in vorticity magnitude. $\nabla\rho\times\nabla p/\rho^2$ represents the baroclinic torque, which generates vorticity when density and pressure gradients are not aligned. $\nabla\times\boldsymbol{F}_{visc}$ denotes viscous dissipation, representing the diffusive effect of vorticity due to viscosity, causing vorticity generation, diffusion, and ultimately dissipation. $\nabla\times\boldsymbol{X}$ on the right-hand side accounts for the contribution of body forces.

Due to the incompressible and ideal nature of the fluid in the current study, the absence of centrifugal forces, conservation of the body force term $\boldsymbol{X}$, negligible effects of the baroclinic torque term, and high Reynolds number flow characteristics, the vorticity dynamics equation can be simplified to:

$$\frac{D\boldsymbol{\omega}}{Dt} = (\boldsymbol{\omega}\cdot\nabla)\boldsymbol{u} \tag{15}$$

In other words, the variation in vorticity was induced primarily by velocity gradients. The velocity gradients aligned with the vorticity lines resulted in vorticity stretching, whereas those perpendicular to the vorticity lines caused vorticity tilting.

The results on the YZ and XZ planes are presented in the following discussion to examine the influence of vorticity stretching on vortex generation. The corresponding vorticity transport equations and related quantities are as follows:

$$(\boldsymbol{\omega}\cdot\nabla)u_x = \omega_{\mathbf{x}}\frac{\partial u_x}{\partial x} + \omega_y\frac{\partial u_x}{\partial y} + \omega_{\mathbf{z}}\frac{\partial u_x}{\partial z} \tag{16}$$

$$(\boldsymbol{\omega}\cdot\nabla)u_y = \omega_{\mathbf{x}}\frac{\partial u_y}{\partial x} + \omega_y\frac{\partial u_y}{\partial y} + \omega_{\mathbf{z}}\frac{\partial u_y}{\partial z} \tag{17}$$

In the context of this case study, where the X- and Y-directional components mainly influenced the velocity gradient, an analysis of the streamwise $(\boldsymbol{\omega}\cdot\nabla)u_x$ and vertical $(\boldsymbol{\omega}\cdot\nabla)u_y$ components of the vorticity stretching term was conducted. Herein:

The contour maps of the streamwise vorticity stretching components $\mathbf{VS}_\mathbf{x}$ and $\mathbf{VS}_\mathbf{y}$ on the YZ plane of the perfect hole are presented in Fig. 13. Overall, from the contour map of the streamwise vorticity stretching components $\mathbf{VS}_\mathbf{x}$ and $\mathbf{VS}_\mathbf{y}$, it is evident that this component exhibits a higher intensity near the exit of the film cooling hole. However, as the flow progressed downstream, the intensity gradually decreased. Both component's primary distributions were concentrated on the cooled wall surface, indicating a correlation with the wall boundary layer.

In Fig. 13. a, at the position behind the film-cooling hole (X/D = 0), the contour map of the vertical vorticity stretching component $\mathbf{VS}_\mathbf{x}$ reveals numerous intertwined alternating and opposing vorticity stretching components, indicating that significant velocity gradients exist between the inflow jet and surrounding fluid at the exit of the film-cooling hole, leading to intense instability and substantial momentum exchange, resulting in strong streamwise vorticity stretching and contraction. This phenomenon occurs in a wide range of cooled wall surfaces. The contour map of the vertical vorticity stretching component $\mathbf{VS}_\mathbf{y}$ at the position behind the film-cooling hole exhibited a similar pattern. The ability of the inflowing jet to penetrate in the normal direction results in a higher distribution range of the vertical vorticity stretching component $\mathbf{VS}_\mathbf{y}$, although it covers a smaller region of the downstream cooled wall.

In Fig. 13. b, the contour map at the trailing edge of the film hole mainly shows its distribution in the cooling-wall region. Positions where Z/D < 0 caused vorticity stretching, whereas at Z/D > 0, it led to vorticity compression. Combining this with the vorticity maps in Fig. 11 at M = 0.6 and X/D = 2, it can be inferred that the vorticity stretching term component primarily influences the vorticity within the wall boundary layer. A contour map of the trailing edge of the film hole (Z/D=0) is shown in Fig. 13. b. The distribution is concentrated around the centre of the wall, with opposite tendencies between the vorticity stretching terms and. The distribution range was higher, resulting in an upward shift of the vortex core in

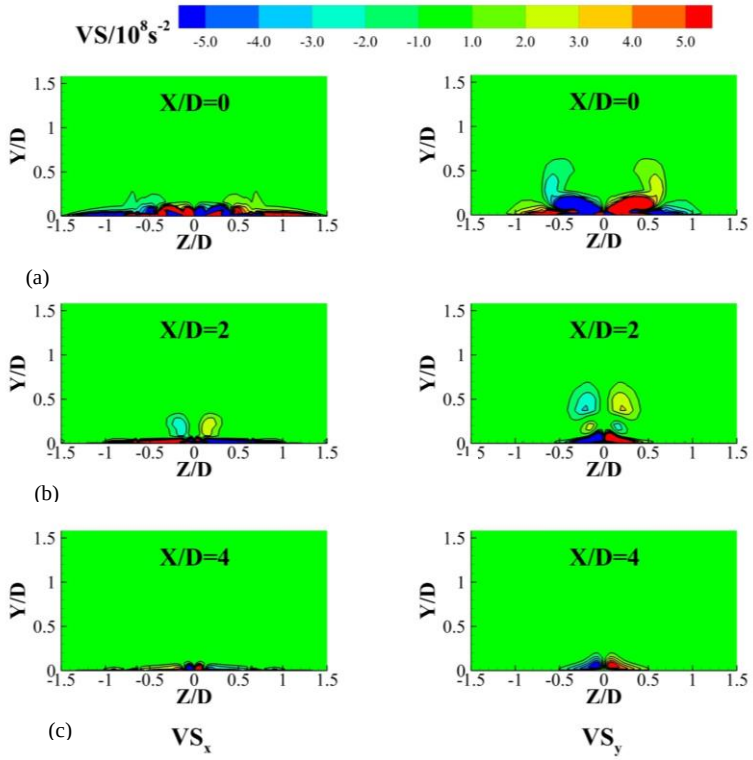

Fig. 13 Contour maps of the vorticity stretching term components VS_x 、 VS_y on the YZ plane of the perfect hole. （left: VS_x ,right: VS_y ）The positions along the streamwise direction are as follows: (a) X/D=0, (b) X/D=2, and (c) X/D=4

the vorticity map, suggesting that the vorticity stretching term primarily influences the kidney-shaped vortex. Similar observations were made for the contour map at Z/D = 0, as shown in Fig. 13. The vorticity stretching term component mainly influences the downstream development of the kidney-shaped vortex. The vorticity stretching term component also influenced the boundary-layer vortices on the wall. As deduced from an earlier analysis, the kidney vortex significantly affected the downstream flow structure and cooling efficiency. Therefore, controlling the vorticity stretching component is crucial.

3.3 Flow Characteristics of Imperfect Holes at Different Blowing Ratios

Analysis of the perfect hole revealed that at a blowing ratio of M = 0.6, the film-cooling efficiency and vortex morphology were relatively optimal. To maintain consistency under the same blowing ratio, we employed the perfect hole scenario as a reference, allowing us to analyse how introducing defective holes alters the flow characteristics. The positions at radial distances X/D = 0.2, 0.6, 1, and 2 are referred to as IT1, IT2, IT3, and IT4, respectively. Figures 14–16 show the velocity distributions in the X-, Y-, and Z-directions at the exit plane for different defect locations. The velocity distribution in the X- and Y-directions follows a pattern in which the velocities increase from left to right in the downstream region, similar to the distribution observed for perfect holes. However, there is a noticeable increase in the velocity near the trailing edge of the film hole, which

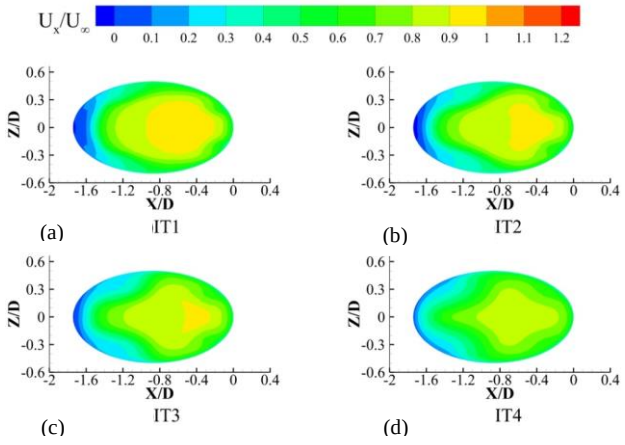

Fig. 14 X-direction Velocity Distribution at Outlet Cross-section for Imperfect Holes at Different Defect Locations

is attributed to the reduced cross-sectional area of the flow owing to the presence of defects, resulting in a distinct velocity enhancement compared to the case of a perfect hole. In addition, the influence of the mainstream turbulent boundary layer on the imperfect hole was more pronounced, leading to a backflow phenomenon at the leading edge of the film hole, evident from the significant reduction in the velocity distribution in the X and Y directions, which diminished as the defect location moved radially away from the film hole. Similarly, the Z-direction velocity in Fig. 16 experienced a significant

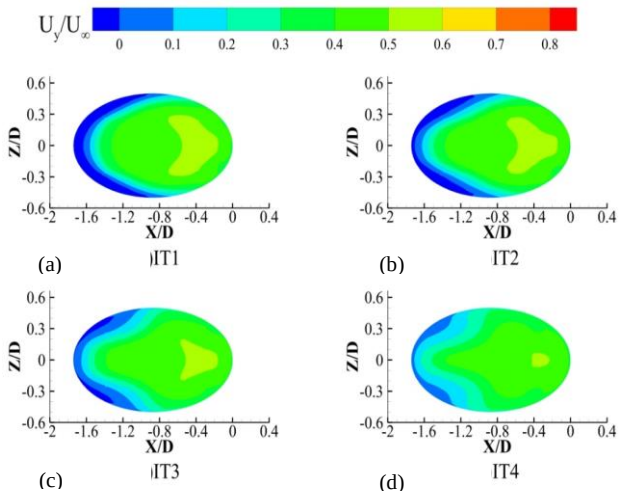

Fig. 15 Y-direction Velocity Distribution at Outlet Cross-section for Imperfect Holes at Different Defect Locations

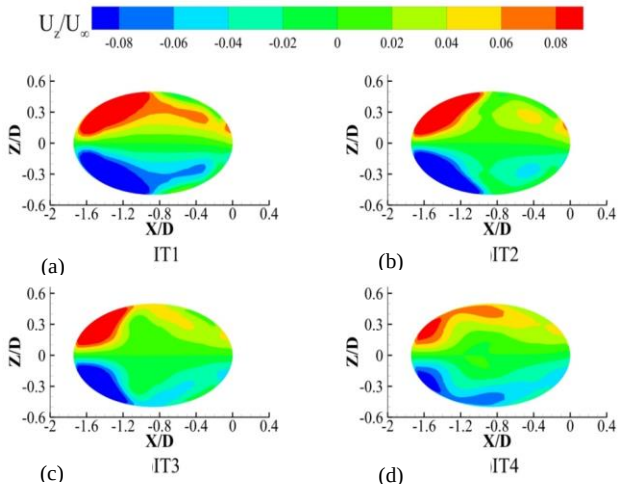

Fig. 16 Z-direction Velocity Distribution at Outlet Cross-section for Imperfect Holes at Different Defect Locations

reduction in magnitude, displaying an irregular and asymmetric distribution compared to the perfect hole. This characteristic likely affected the formation of kidney-shaped vortices. Furthermore, the defect location significantly affects the velocities in the film hole exit region. As the defect moved radially away from the film hole, the magnitudes of the X-, Y-, and Z-direction velocities decreased.

The streamline and temperature contour maps at the downstream cross sections X/D = 1, 3, and 5 for various defect locations are presented in Fig. 17. Compared to the perfect hole case at M=0.6, it is evident that the imperfect holes exhibit similar characteristics. Kidney vortices formed at different blowing ratios and gradually detached from the wall as the flow progressed downstream. Furthermore, the intensity of the kidney vortices increased with the blowing ratio. However, defects in the film holes enhanced the strength of the downstream kidney-shaped vortices, disrupting their symmetrical distribution and causing them to deflect asymmetrically, which correlated with the previously observed significant increase in the Y-direction velocity. At defect locations IT1 and IT2, the development of kidney vortices led to the formation of suction zones at the X/D=1 position, subsequently evolving into two distinct and unequal elliptical distributions as the positions of the vortex pairs increased. In contrast, the suction effect weakened at defect locations IT3 and IT4, and the separation phenomenon diminished, resulting in a more coherent semicircular distribution. Undoubtedly, this enhanced the efficiency of film cooling.

3.4 Efficiency of Film Cooling

The vortex structure in the downstream flow field of the film-cooling hole significantly affected the wall film cooling efficiency. This section analyses the wall film cooling efficiency contour maps and spanwise-averaged film cooling efficiency.

Figure 18 shows the wall film cooling efficiency contour maps for a perfect hole at various blowing ratios. Figure 19 shows the spanwise-averaged film-cooling efficiency. The contour maps of the film-cooling efficiency reveal a clear trend: as the blowing ratio increases, the film-cooling efficiency gradually decreases. This decrease was attributed to the increased Y-direction velocity, which resulted in a higher penetration ability of the inlet flow. Similarly, the spanwise-averaged film cooling efficiency along the flow direction decreased in the upstream front

region (X/D < 15) with an increasing blowing ratio. However, in the downstream rear region, the spanwise-averaged efficiency decreased for a low blowing ratio (M = 0.3), whereas the spanwise-averaged efficiency gradually increased for other blowing ratios. Notably, the spanwise-averaged efficiency for M = 0.6 and M = 0.9 surpasses that of M = 1.2. This phenomenon is attributed to reattachment at higher blowing ratios, which enhances the spanwise film-cooling efficiency.

Figure 20 shows the defective hole's wall surface film cooling effectiveness distribution at M = 0.6 and different defect positions. Figure 21 shows the defective hole's wall surface average film cooling effectiveness at M = 0.6 and different defect positions. Observing the film cooling effectiveness distribution cloud maps, it is evident that in the vicinity of the cooling hole (X/D<5), as the defect position moves radially away from the cooling hole, the film cooling effectiveness gradually increases. The highest film cooling effectiveness is achieved in the near-hole region of the defect position IT4. Compared to the perfect hole at M = 0.6, a significant enhancement in cooling effectiveness can be observed. Similarly, observing the wall surface average film cooling effectiveness in the downstream near-hole region (X/D < 5), the average film cooling effectiveness gradually increases as the defect position moves radially away from the cooling hole. However, in the downstream far-hole region, except for defect position IT1, where the reattachment phenomenon occurs, leading to an increase in the average film cooling effectiveness, defect positions IT3 and IT4 maintain relatively low values in terms of the

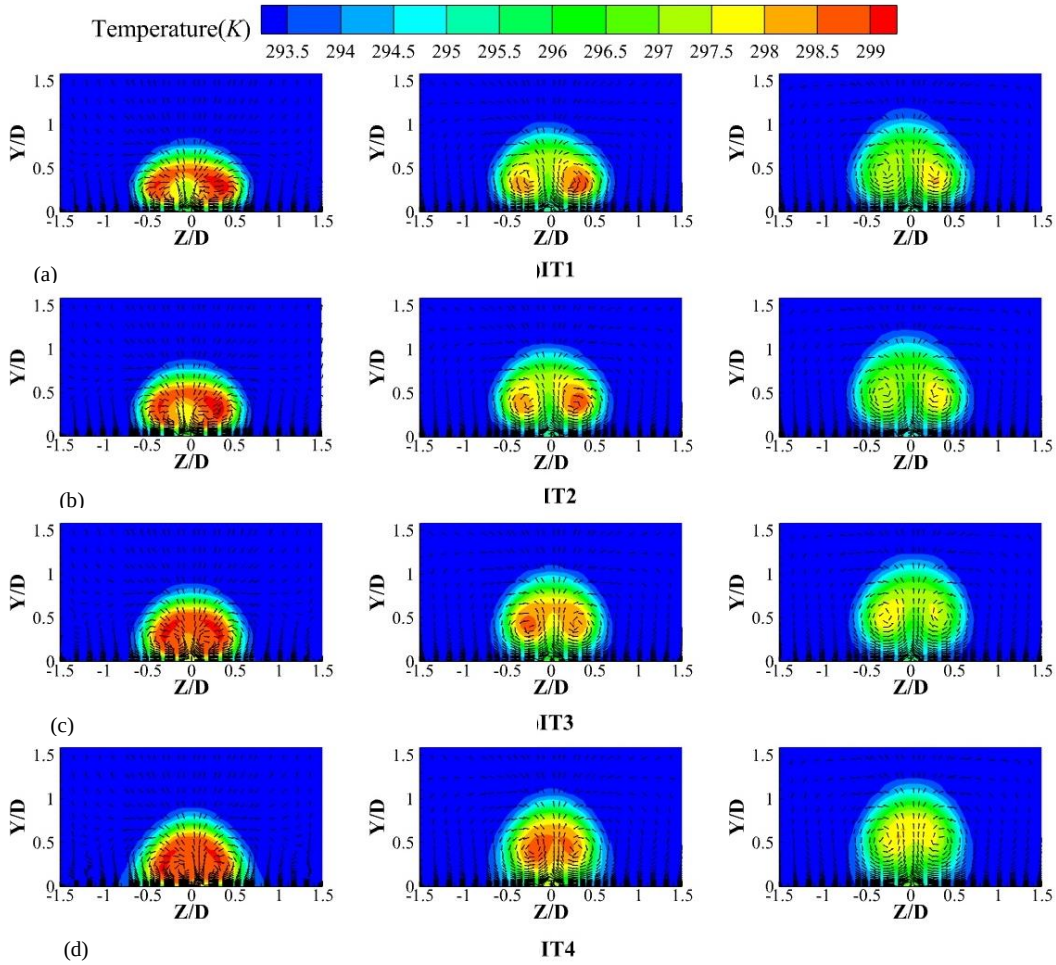

Fig. 17 Velocity vector and temperature distribution contour maps at downstream sections for the flawed hole at different flaw positions (a: X/D=1, b: X/D=3, X/D=5)

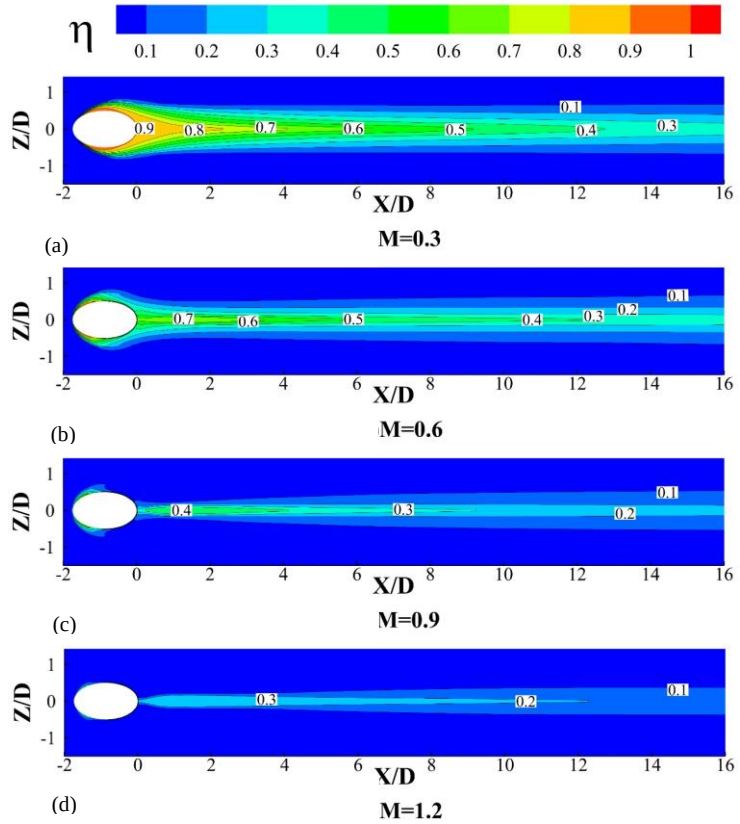

Fig. 18 Contour maps of wall film cooling efficiency for the perfect hole at different blowing ratios

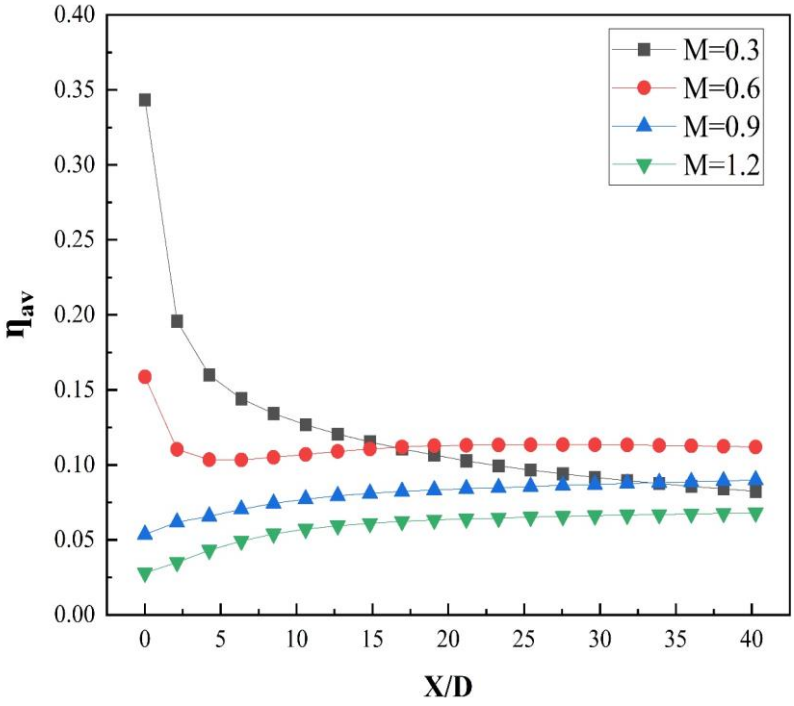

Fig. 19 Wall-averaged spanwise film cooling efficiency for the perfect hole at different blowing ratios

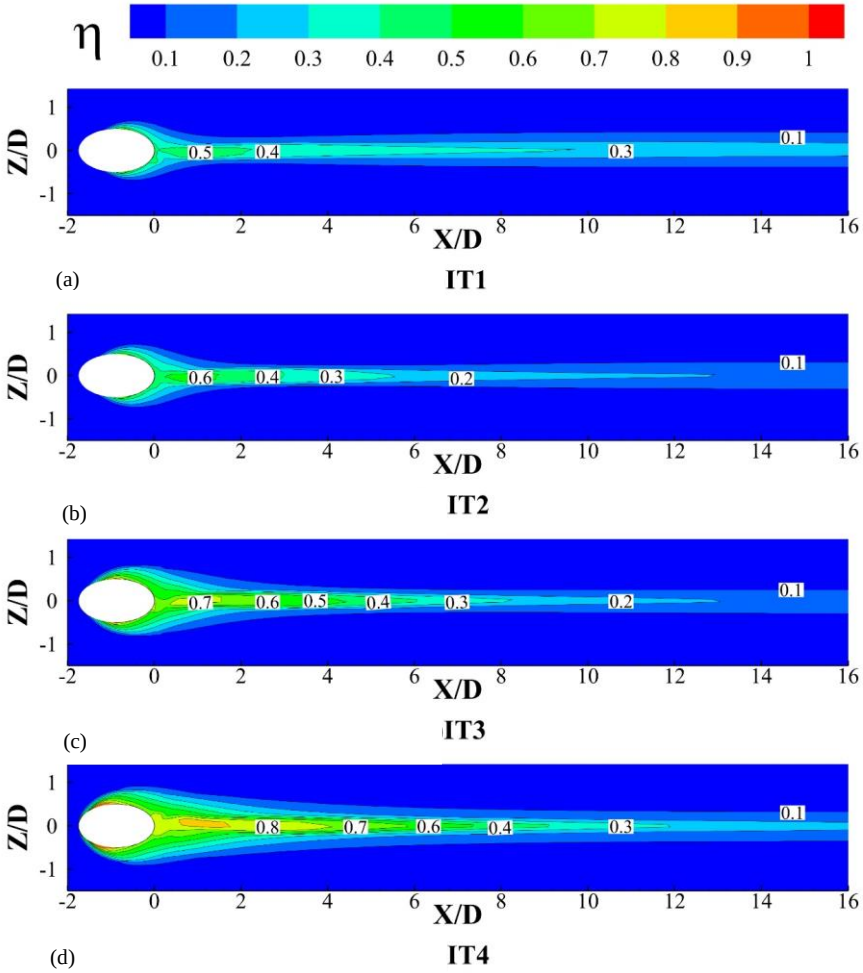

Fig. 20 Contour maps of wall film cooling efficiency for the imperfect hole at different defect positions under M=0.6

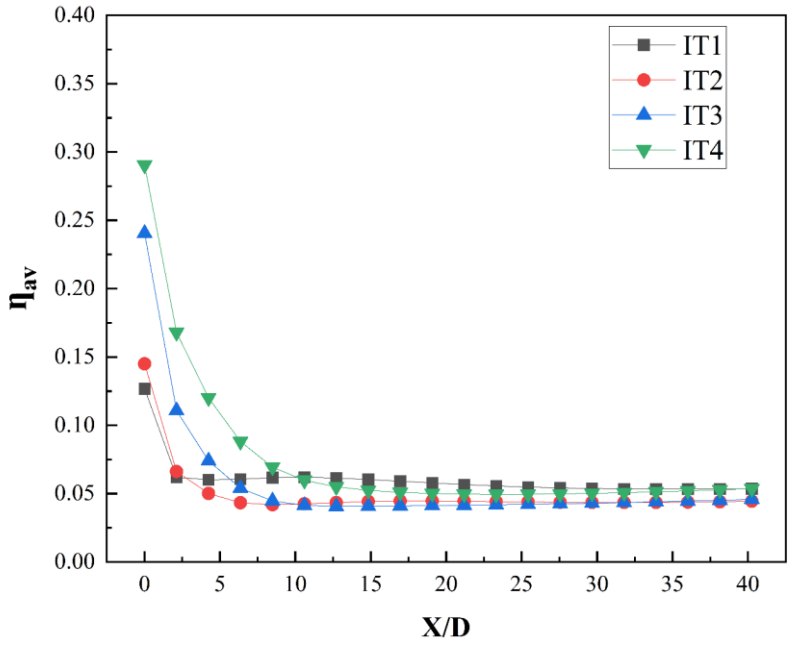

Fig. 21 Wall-averaged spanwise film cooling efficiency for the imperfect hole at different defect positions under M=0.6

wall surface average film cooling effectiveness. Defect position IT4 consistently maintains a favourable wall surface average film cooling effectiveness. In conclusion, an increase in the blowing ratio reduces wall surface film cooling effectiveness, while the spanwise wall surface film cooling effectiveness changes due to the reattachment phenomenon. In the near-hole region, defect position IT4 yields the best results in both wall surface film cooling effectiveness and spanwise wall surface average film cooling effectiveness.

4. CONCLUSION

This study conducts numerical investigations on the flow characteristics of a perfect film-cooling hole under four different blowing ratios. Vortex structures were generated using vortex kinematics. Additionally, the flow characteristics of the defective film-cooling hole were analysed at an optimal blowing ratio of M = 0.6, and a comparison was made with a perfect hole. Finally, the combined effects of these factors on the film-cooling efficiency were examined, leading to the following conclusions.

(1) The interaction between the mainstream and incoming flows in the inlet region results in a velocity distribution at the exit of the perfect film-cooling hole, influenced primarily by the X- and Y-component velocities. Moreover, the velocity in the exit region gradually increased. With an increase in the blowing ratio, the amplified Y-component velocity enhanced the incoming flow's penetration, resulting in reattachment phenomena and a deteriorated cooling performance. Simultaneously, the kidney vortex generated downstream of the film-cooling hole detaches from the wall as the flow progresses, diminishing the cooling effectiveness. An increase in the blowing ratio further exacerbated the suction effect.

(2) The strength of the kidney-shaped vortex in the perfect film-cooling hole gradually decreased as the flow progressed. With an increase in the blowing ratio, the vortex strength intensified, accompanied by an increase in the position of the vortex centre. For higher blowing ratios, a higher vortex centre position results in a slower decline in the cooling efficiency. Conversely, at lower blowing ratios, the vortex centre position decreases, leading to an enhanced decline in efficiency. The formation of the kidney vortex primarily arises from the interaction between the mainstream and impinging jets, which generates shear-layer vortices. This phenomenon is influenced primarily by the vortex-stretching term component, in which the same component affects the boundary layer vortices.

(3) At the optimal blowing ratio of M=0.6, the velocity distribution pattern for the imperfect film-cooling hole was similar to that for the perfect hole, with comparable distribution trends. However, because of the reduced flow cross-sectional area at the defect, the velocities increased noticeably, further affecting the distribution pattern of the kidney vortex. Additionally, pronounced backflow phenomena occurred at defect positions IT1 and IT2, whereas these backflow effects diminished notably at positions IT3 and IT4.

(4) As the blowing ratio increased, the wall-film cooling efficiency of the perfect hole gradually decreased. Similarly, the wall-averaged film cooling efficiency along the flow direction diminishes in the downstream front region but gradually increases for blowing ratios of 0.6, 0.9, and 1.2. The wall-averaged film cooling efficiency was highest at a 0.6-blowing ratio.

At a blowing ratio of M = 0.6, as the defect location moved radially away from the film cooling hole, the wall film cooling efficiency progressively increased. The highest wall-film cooling efficiency was achieved at defect position IT4, surpassing the film-cooling efficiency of a perfect hole at M=0.6. This trend was similar for the wall-averaged film-cooling efficiency, which increased as the defect position moved radially away from the film-cooling hole. Defect position IT4 consistently maintained a favourable wall-averaged film-cooling efficiency throughout the process. Overall, compared with the near-hole region of the perfect hole, the defect position IT4 yields a superior film-cooling efficiency.

ACKNOWLEDGEMENTS

The authors wish to thank the support of Zhejiang Province Public Welfare Technology Applicaiton Research Project (No. LGG19A020002).

CONFLICT OF INTEREST

The authors declare that they have no known competing financial interests or personal relationships that could have appeared to influence the work reported in this paper.

AUTHORS CONTRIBUTION

Ruoling Dong proposed the framework and methodology of this study. **Shuang Liang** conducted numerical simulation experiments and validation with the assistance of **Wanwen Xu**. **Shuang Liang** analyzed the data using software, under the guidance of **Youqiang Wei**. **Shuang Liang** drafted the manuscript and received review and editing from **Ruoling Dong**. All authors have read and agreed to the published version of the manuscript.

REFERENCES

Andreopoulos, J., & Rodi, W. (1984). Experimental investigation of jets in a crossflow. *Journal of Fluid Mechanics*, *138*, 93–127. https://doi.org/10.1017/S0022112084000057

Bunker, R. S. (2005). A review of shaped hole turbine film-cooling technology. *Journal of Heat Transfer*, *127*(4), 441–453. https://doi.org/10.1115/1.1860562

Bunker, R. S. (2014, August 4). *Effect of partial coating blockage on film cooling effectiveness.* ASME Turbo Expo 2000: Power for Land, Sea, and Air. https://doi.org/10.1115/2000-GT-0244

Chang, J., Du, Y., Zheng, S., Duan, X., & Liu, Y. (2019). Performance analysis of different influencing factors on film cooling and the internal relations with vortex structures. *AIP Advances*, *9*(7), 070701. https://doi.org/10.1063/1.5110726

Chen, Z., Zhang, Z., Li, Y., Su, X., & Yuan, X. (2019). Vortex dynamics based analysis of internal crossflow effect on film cooling performance. *International Journal of Heat and Mass Transfer*, *145*, 118757. https://doi.org/10.1016/j.ijheatmasstransfer.2019.118757

Funazaki, K., Kawabata, H., Takahashi, D., & Okita, Y. (2013). *Experimental and Numerical Studies on Leading Edge Film Cooling Performance: Effects of Hole Exit Shape and Freestream Turbulence.* 1223–1233. https://doi.org/10.1115/GT2012-68217

Han, J. C., Dutta, S., & Ekkad, S. (2013). Gas *turbine heat transfer and cooling technology* (2nd ed.). CRC Press. https://doi.org/10.1201/b13616

Heidmann, J. D., & Ekkad, S. (2008). A novel antivortex turbine film-cooling hole concept. *Journal of Turbomachinery*, *130*(031020). https://doi.org/10.1115/1.2777194

Huang, K., Zhang, J., Tan, X., & Shan, Y. (2018). Experimental study on film cooling performance of imperfect holes. *Chinese Journal of Aeronautics*, *31*(6), 1215–1221. https://doi.org/10.1016/j.cja.2018.04.001

Jiang, Y. T., Deng, H. F., You, X. L., Zhao, H. J., & Yue, G. Q. (2020). Numerical investigation on film cooling mechanism with different coolant delivery configurations. *Journal of Applied Fluid Mechanics*, *14*(1), 175–185. https://doi.org/10.47176/jafm.14.01.31345

Jovanovic´, M. B., de Lange, H. C., & van Steenhoven, A. A. (2005). *Influence of laser drilling imperfection on film cooling performances*. Turbo, Parts A and B, 285–292. https://doi.org/10.1115/GT2005-68251

Jovanović, M. B., de Lange, H. C., & van Steenhoven, A. A. (2006). Influence of hole imperfection on jet cross flow interaction. *International Journal of Heat and Fluid Flow*, *27*(1), 42–53. https://doi.org/10.1016/j.ijheatfluidflow.2005.06.003

Jovanović, M. B., de Lange, H. C., & van Steenhoven, A. A. (2008). Effect of hole imperfection on adiabatic film cooling effectiveness. *International Journal of Heat and Fluid Flow*, *29*(2), 377–386. https://doi.org/10.1016/j.ijheatfluidflow.2007.11.008

Lim, T. T., New, T. H., & Luo, S. C. (2001). On the development of large-scale structures of a jet normal to a cross flow. *Physics of Fluids*, *13*(3), 770–775. https://doi.org/10.1063/1.1347960

Lakehal, D., Theodoridis, G. S., & Rodi, W. (2001). Three-dimensional flow and heat transfer calculations of film cooling at the leading edge of a symmetrical turbine blade model. *International Journal of Heat and Fluid Flow*, *22*(2), 113–122. https://doi.org/10.1016/S0142-727X(00)00084-9

Nemdili, F., Azzi, A., & Jubran, B. A. (2011). Numerical investigation of the influence of a hole imperfection on film cooling effectiveness. *International Journal of Numerical Methods for Heat & Fluid Flow*, *21*(1),

46–60. https://doi.org/10.1108/09615531111095067

Panda, R. K., Pujari, A. K., & Gudla, B. (2023). A Comparative study of film cooling with combined impingement and film cooling. *Journal of Applied Fluid Mechanics*, *16*(7), 1386–1401. https://doi.org/10.47176/jafm.16.07.1669

Rezzag, T., & Jubran, B. A. (2019b, June 17). *A numerical study on the effect of hole inclination angle with imperfection on film cooling effectiveness*. GT2019. https://doi.org/10.1115/GT2019-90490

Sykes, R. I., Lewellen, W. S., & Parker, S. F. (1986). On the vorticity dynamics of a turbulent jet in a crossflow. *Journal of Fluid Mechanics*, *168*, 393–413. https://doi.org/10.1017/S0022112086000435

Tian, K., Wang, J., Liu, C., Yang, L., & Sundén, B. (2018). Effect of blockage configuration on film cooling with and without mist injection. *Energy*, *153*, 661–670. https://doi.org/10.1016/j.energy.2018.04.050

Walters, D. K., & Leylek, J. H. (1997). A detailed analysis of film-cooling physics: part I—Streamwise injection with cylindrical holes. *Journal of Turbomachinery*, *122*(1), 102–112. https://doi.org/10.1115/1.555433

Wu, H., Cheng, H., Li, Y., Rong, C., & Ding, S. (2016). Effects of side hole position and blowing ratio on sister hole film cooling performance in a flat plate. *Applied Thermal Engineering*, *93*, 718–730. https://doi.org/10.1016/j.applthermaleng.2015.09.118

Zhan, J., Li, Y., Wai, W. O., & Hu, W. (2019). Comparison between the Q criterion and Rortex in the application of an in-stream structure. *Physics of Fluids*, *31*(12), 121701. https://doi.org/10.1063/1.5124245

Zhang, J., Zhang, S., Wang, C., & Tan, X. (2020). Recent advances in film cooling enhancement: A review. *Chinese Journal of Aeronautics*, S1000936120300972. https://doi.org/10.1016/j.cja.2019.12.023

Zhang, W., & Zhu, H. R. (2020). Film cooling performance of the staggered arrangement of auxiliary holes and main holes on a flat plate. Journal *of Applied Fluid Mechanics*, *14*(3), 741–752. https://doi.org/10.47176/jafm.14.03.31933